J. Fluid Mech. (2001), *vol.* 428, *pp.* 133–148. Printed in the United Kingdom

Topology of vortex breakdown bubbles in a cylinder with a rotating bottom and a free surface

By MORTEN BRØNS[1], LARS K. VOIGT[2] AND JENS N. SØRENSEN[2]

[1]Department of Mathematics, Technical University of Denmark, DK-2800 Kongens Lyngby, Denmark

[2]Department of Energy Engineering, Technical University of Denmark, DK-2800 Kongens Lyngby, Denmark

(Received 22 April 2000 and in revised form 11 July 2000)

The flow patterns in the steady, viscous flow in a cylinder with a rotating bottom and a free surface are investigated by a combination of topological and numerical methods. Assuming the flow is axisymmetric, we derive a list of possible bifurcations of streamline structures on varying two parameters, the Reynolds number and the aspect ratio of the cylinder. Using this theory we systematically perform numerical simulations to obtain the bifurcation diagram. The stability limit for steady flow is found and established as a Hopf bifurcation. We compare with the experiments by Spohn, Mory & Hopfinger (1993) and find both similarities and differences.

1. Introduction

The fluid motion in a cylinder generated by a rotating cover has proved to be a useful tool for the study of secondary structures on a basic vortex flow. Experimental investigations by Vogel (1968), Ronnenberg (1977), and Escudier (1984) have shown that several recirculation bubbles may exist on the main vortex axis and that the flow in the steady regime is axisymmetric to a high degree of accuracy. The axisymmetry allows efficient computational studies to be performed, and as shown by e.g. Sørensen & Loc (1989), Lopez (1990), and Tsitverblit (1993) good agreement with visualization experiments can be obtained.

A number of variations of the basic configuration with one fixed and one rotating cover have been studied, both experimentally and computationally. The fixed cover has been replaced by a rotating cover (Valentine & Jahnke 1994; Gelfgat, Bar-Yoseph & Solan 1996*a*, *b*, *c*; Jahnke & Valentine 1998), a non-Newtonian fluid has been used (Escudier & Cullen 1996; Xue, Phan-Thien & Tanner 1999), a rod has been added at the axis (Mullin *et al.* 2000), the flat rotating bottom cover has been replaced by a cone (Pereira & Sousa 1999), and the fixed top cover has been replaced by a free surface (Spohn, Mory & Hopfinger 1993; Lopez & Chen 1998). All these studies show a large set of flow structures which are quite sensitive to variations of external parameters.

In the present paper we present a classification of the flow structures that exist in the steady domain for the configuration with a free surface on varying the two

parameters, Reynolds number and aspect ratio of the cylinder,

$$Re = \frac{\Omega R^2}{\nu}, \quad h = \frac{H}{R}. \tag{1}$$

Here Ω is the angular velocity of the bottom cover, H, R are the height and radius of the cylinder respectively, and ν is the kinematic viscosity. The main aim is to describe the structures in the parameter range considered experimentally by Spohn *et al.* (1993). We obtain partial agreement as well as discrepancies, and also find details that have not been resolved in the experiment.

Our approach is topological, that is, we consider the streamlines as trajectories for the velocity field and apply methods from bifurcation theory to describe the qualitative changes that are possible. We have previously (Brøns, Voigt & Sørensen 1999) used this idea to classify the patterns in the case with two solid covers, utilizing the theory for bifurcation of patterns close to the cylinder axis developed by Brøns (1999). Here we extend the theory to include bifurcations occuring close to both the axis and the surface. We then use the topological apparatus to systematically extract features of the flow patterns obtained from numerical simulations to construct the bifurcation diagram. The richness of the problem is apparent from figure 1 which shows the set of topologies we have encountered.

We assume the free surface to be flat, a reasonable assumption if the Froude number is small as in the experiments by Spohn *et al.* (1993). Further, we neglect any surface tension effects, so the surface is a pure slip boundary. With these assumptions, the flow is identical to the flow in the lower half part of a cylinder with two solid covers, both rotating with the same angular velocity.

To our knowledge, the flow structures in the case of the free surface has only been considered experimentally by Spohn *et al.* (1993). For the equivalent case with a co-rotating cover our results corroborates and extend the results by Valentine & Jahnke (1994) and Gelfgat *et al.* (1996*a*, *c*).

As also established by Gelfgat *et al.* (1996*b*) the bifurcations of the structures we consider are of a pure topological nature, and are not related to changes in stability of the steady flow. However, to locate the parameter region where the analysis is valid we also determine the stability limit for the steady flow. As is well-known for the flow with a rigid cover (Daube & Sørensen 1989), the loss of stability happens through a Hopf bifurcation.

The paper is organized as follows. In § 2 we derive the topological classification theory. In § 3 the numerical method is presented and validated, and in § 4 the bifurcation diagram is established and compared with experimental results. Finally, conclusions are drawn in § 5.

2. Streamline topology of axisymmetric flow

2.1. *Bifurcations on the axis*

Axisymmetric flows can be described using cylindrical coordinates (r, θ, z) with the corresponding velocity field $\boldsymbol{v} = (u, v, w)$ depending only on r, z. A stream function $\psi(r, z)$ can be defined such that

$$u = \frac{1}{r}\frac{\partial \psi}{\partial z}, \quad w = \frac{1}{r}\frac{\partial \psi}{\partial r}. \tag{2}$$

We are interested in the topology of the system of contours of ψ. Using $\rho = r^2/2$ as a radial variable puts the differential equations for the contours into Hamiltonian

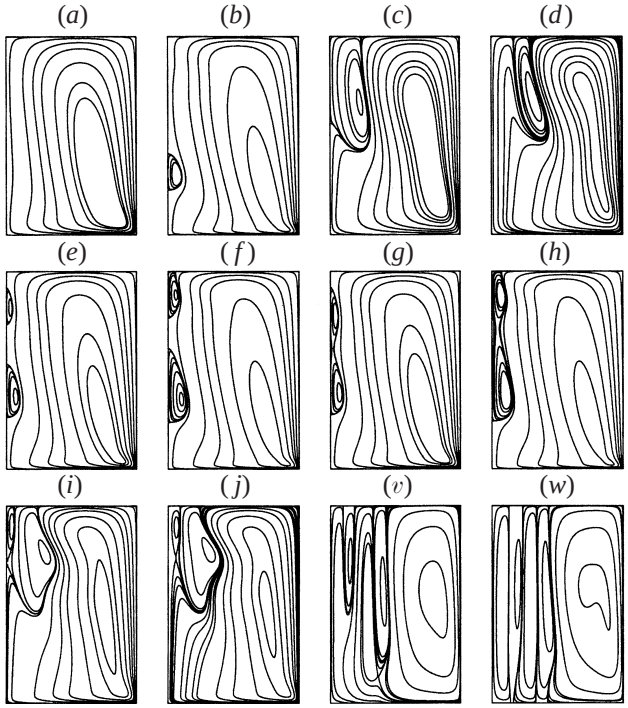

FIGURE 1. Typical representatives of the observed flow topologies (contours of the stream function) found in the steady domain. The drawings are scaled to the same normalized aspect ratio. Only the right half of a meridional plane is shown. The vertical line to the left is the axis. (*a*) $Re = 1000$, $h = 2.0$, no bubble. (*b*) $Re = 2800$, $h = 4.0$, axis bubble. (*c*) $Re = 1000$, $h = 1.0$, corner bubble. (*d*) $Re = 1700$, $h = 1.0$, surface bubble. (*e*) $Re = 1950$, $h = 3.0$, two axis bubbles. (*f*) $Re = 3000$, $h = 4.0$, one axis bubble and one corner bubble. (*g*) $Re = 1700$, $h = 2.7$, axis bubble with inner structure. (*h*) $Re = 3100$, $h = 4.0$, corner bubble with inner structure. (*i*) $Re = 2500$, $h = 1.9$, corner bubble with inner corner bubble. (*j*) $Re = 2800$, $h = 2.0$, surface bubble and in-flow saddle loop. (*v*) $Re = 1500$, $h = 0.3$, transition towards multi-cell topology. (*w*) $Re = 2100$, $h = 0.3$, Multi-cell topology with separatrices joining stagnation points at the surface and bottom. The latter two topologies are not covered by the present analysis.

form,

$$\dot{\rho} = ru = \frac{\partial \psi}{\partial z}, \quad \dot{z} = w = -\frac{\partial \psi}{\partial \rho}. \tag{3}$$

Since the present problem is characterized by two parameters, our interest is concentrated on bifurcation of codimension up to two, that is, bifurcations that can occur persistently in systems of the form (3) where ψ depends on up to two parameters.

Topologies and bifurcations of structures close to the axis at a point away from the surface have been treated in detail by Brøns (1999) and Brøns *et al.* (1999). The relevant results are reviewed in figure 2. A regular critical point (a hyperbolic saddle) is structurally stable. Two kinds of bifurcations of codimension-one exist: bubble creation and bubble merging. The one possible codimension-two diagram consists of three codimension-one curves meeting in the codimension-two point. These are a bubble creation curve, a bubble merging curve, and a cusp bifurcation curve, that is, the merging/creation of a centre and a saddle away from the axis, see Brøns & Hartnack (1999).

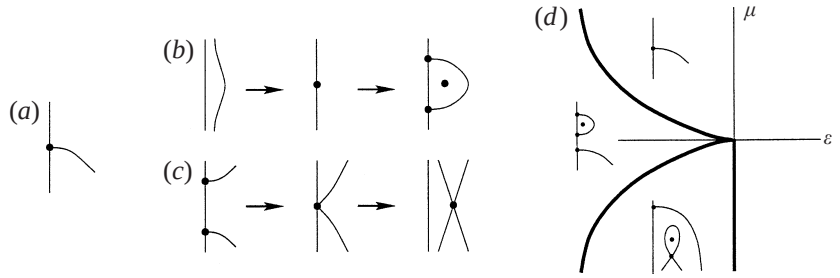

FIGURE 2. Local flow patterns and bifurcations close to the axis or the surface. (*a*) Regular critical point. (*b*, *c*) Topology changes of codimension-one obtained by varying a parameter through a degenerate configuration: (*b*) bubble creation, (*c*) bubble merging. (*d*) Codimension-two bifurcation shown in a parameter plane where the parameters are denoted (ε, μ).

In the system (3) the variables ρ and z occur symmetrically. This means that the variables may be interchanged, and in the topologies in figure 2 the axis can also play the role of the surface. Brøns (1994) also finds these bifurcations in flows close to the surface. A difference in the interpretation of the critical points in the two cases should be noted, however. A critical point for ψ on the axis corresponds to a stagnation point on the axis in the cylinder. A critical point on the surface corresponds to a circular streamline embedded in the surface. Such critical points are denoted 'periodic points' by Valentine & Jahnke (1994).

The results are based on an expansion of ψ in a Taylor series at a point on the axis, taken to be the origin,

$$\psi = \rho \sum_{n+m=0}^{\infty} a_{n+1m} \rho^n z^m, \tag{4}$$

where the factor ρ accounts for the axis being a streamline. To study structures close to both the axis and the surface, the relevant expansion is

$$\psi = \rho z \sum_{n+m=0}^{\infty} a_{n+1m+1} \rho^n z^m \tag{5}$$

which reflects that both the axis and the surface (which we here choose to be $z = 0$) are contours of ψ. The bifurcation analysis for this case has not been performed before and is the subject of the following. For simplicity we denote the origin – the intersection of the axis with the surface – as the *corner*, and let the fluid region below the surface be $\rho \geqslant 0, z \leqslant 0$.

2.2. *Bifurcations close to the corner*

Including terms to second order in (5) yields the linearized equations for the contours,

$$\dot{\rho} = a_{11}\rho, \quad \dot{z} = -a_{11} z. \tag{6}$$

If $a_{11} \neq 0$, the corner is a regular saddle point, figure 3. The direction of the flow depends on the sign of a_{11}. If $a_{11} = 0$, the corner is a degenerate critical point, and higher-order terms are decisive. To find the codimension-one bifurcations as a_{11} goes through zero, we rename a_{11} as ε to display it is a small parameter and consider the cubic approximation of ψ, yielding

$$\dot{\rho} = \rho(\varepsilon + a_{21}\rho + 2a_{12} z), \quad \dot{z} = -z(\varepsilon + 2a_{21}\rho + a_{12} z), \tag{7}$$

where we assume a_{12}, a_{21} both non-zero.

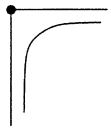

FIGURE 3. A regular critical point in the corner.

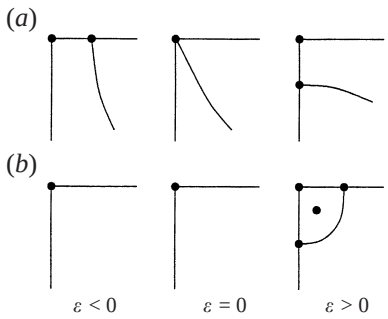

FIGURE 4. Codimension-one bifurcations at the corner for $a_{12} > 0$. (*a*) $a_{21} > 0$, corner crossing bifurcation. (*b*) $a_{21} < 0$, corner bubble creation. The same bifurcations occur for $a_{12} < 0$ but in reverse order in ε.

The system has a critical point on the axis ($\rho = 0$) at $z = -\varepsilon/a_{12}$, a critical point on the surface ($z = 0$) at $\rho = -\varepsilon/a_{21}$, and an in-flow critical point at

$$\rho = -\frac{\varepsilon}{3a_{21}}, \quad z = -\frac{\varepsilon}{3a_{12}}. \tag{8}$$

The bifurcation diagrams are shown in figure 4. In case (*a*) a critical point crosses the corner, in (*b*) a corner bubble is created/destroyed.

A codimension-two situation occurs if, in addition to $a_{11} = 0$, one of a_{12}, a_{21} is also zero. We consider the case $a_{12} = 0$ but $a_{21} \neq 0$. To find the bifurcations as the degenerate parameters are close to zero, we rename them

$$\tilde{\varepsilon} = a_{11}, \quad \tilde{\mu} = a_{12} \tag{9}$$

and first simplify the equations slightly by a coordinate transformation to a nonlinear normal form, following Brøns (1999) and Brøns & Hartnack (1999). The new coordinates (x, y) are found from a canonical transformation defined by the generating function

$$S = \sum_{k+l+n+m=3} s_{klmn} \tilde{\varepsilon}^k \tilde{\mu}^l \rho^n y^m \tag{10}$$

such that

$$x = \frac{\partial S}{\partial y}, \quad z = \frac{\partial S}{\partial \rho}. \tag{11}$$

For an introduction to canonical transformations using generating functions, see e.g. Goldstein (1950). The specific choice of S ensures that (11) defines an almost-identity coordinate transformation for any choice of the s_{klmn}. Indeed, solving (11) for x, y and

including terms up to the second order yields

$$\left.\begin{aligned} x &= \rho + 2s_{1200}\rho z + s_{2100}\rho^2 + s_{1101}\rho\tilde{\mu} + s_{1110}\rho\tilde{\varepsilon} + 2s_{0210}z\tilde{\varepsilon} \\ &\quad + s_{0111}\tilde{\varepsilon}\tilde{\mu} + s_{0120}\tilde{\varepsilon}^2 + 3s_{0300}z^2 + 2s_{0201}z\tilde{\mu} + s_{0102}\tilde{\mu}^2, \\ y &= z - s_{1200}z^2 - s_{1101}z\tilde{\mu} - s_{1002}\tilde{\mu}^2 - s_{1110}z\tilde{\varepsilon} - s_{1011}\tilde{\varepsilon}\tilde{\mu} \\ &\quad - s_{1020}\tilde{\varepsilon}^2 - 2s_{2100}\rho z - 2s_{2001}\rho\tilde{\mu} - 2s_{2010}\rho\tilde{\varepsilon} - 3s_{3000}\rho^2. \end{aligned}\right\} \tag{12}$$

As the topology of the contours of ψ is unchanged under a smooth coordinate transformation, we are free to choose the s_{klmn} to make the transformed ψ as simple as possible. First we require that the transformation preserves the boundaries, i.e. $\rho = 0$ is mapped to $x = 0$ and $z = 0$ is mapped to $y = 0$. This forces a number of the s_{klmn} to be zero. Using this, insertion of (12) in the expansion (5) and truncating after the fourth order results in

$$\begin{aligned} \psi = xy(&\tilde{\varepsilon} + (a_{21} + s_{2100}\tilde{\varepsilon})x + (\tilde{\mu} - s_{1200}\tilde{\varepsilon})y \\ &+ (a_{31} + s_{2100}a_{21})x^2 + (a_{22} - s_{1200}a_{21})xy + a_{13}y^2). \end{aligned} \tag{13}$$

With the choice

$$s_{2100} = -\frac{a_{31}}{a_{21}}, \quad s_{1200} = \frac{a_{22}}{a_{21}}, \tag{14}$$

the x^3y and x^2y^2 terms disappear and we obtain

$$\psi = xy\left(\tilde{\varepsilon} + \left(a_{21} - \frac{a_{31}}{a_{21}}\tilde{\varepsilon}\right)x + \left(\tilde{\mu} - \frac{a_{22}}{a_{21}}\tilde{\varepsilon}\right)y + a_{13}y^2\right). \tag{15}$$

Finally, with the added non-degeneracy condition $a_{13} \neq 0$, we can divide ψ by a_{13}, since multiplying ψ by a constant does not modify the set of contours, only the specific value of ψ along a given curve. This results in the normal form

$$\psi = xy(\varepsilon + b_{21}x + \mu y + y^2) \tag{16}$$

with

$$\varepsilon = \frac{\tilde{\varepsilon}}{a_{13}}, \quad b_{21} = \frac{a_{21}^2 - a_{31}\tilde{\varepsilon}}{a_{21}a_{13}}, \quad \mu = \frac{a_{21}\tilde{\mu} - a_{22}\tilde{\varepsilon}}{a_{21}a_{13}}. \tag{17}$$

The (ε, μ) parameter space will be partitioned by curves of codimension-one bifurcations. We proceed by determining these curves for each of the possible types. In each case, the condition for bifurcation is that a critical point (x_c, y_c) exists with a singular Jacobian, that is

$$\psi_x(x_c, y_c) = 0, \quad \psi_y(x_c, y_c) = 0, \quad -\psi_{xy}(x_c, y_c)^2 + \psi_{xx}(x_c, y_c)\psi_{yy}(x_c, y_c) = 0, \tag{18}$$

where the subscripts denote differentiation.

For bifurcations in the corner, $(x_c, y_c) = (0, 0)$. Inserting this in (18) with ψ given by (16) makes the first two conditions identically fulfilled and the last condition yields $\varepsilon = 0$. According to the previous analysis, the type of bifurcation is determined by the sign of a_{21} in the expansion (5), that is, by the sign of $\psi_{xxy}(0, 0)$. The non-degeneracy condition is $a_{12} = \psi_{xyy}(0, 0) \neq 0$. We obtain

$$\psi_{xxy}(0, 0) = 2b_{21}, \quad \psi_{xyy}(0, 0) = 2\mu. \tag{19}$$

We conclude that the bifurcation at $\varepsilon = 0$ for $\mu \neq 0$ is a corner crossing if μ and b_{21} have the same sign, and a corner bubble creation if μ and b_{21} have opposite sign.

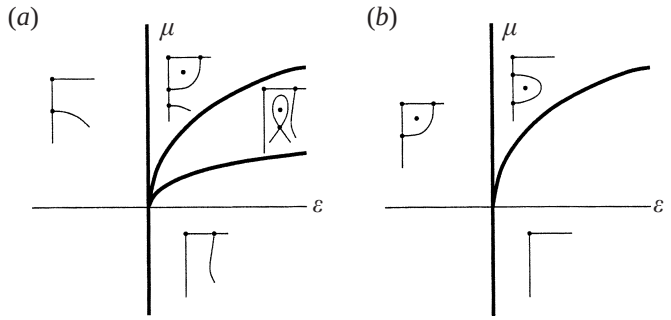

FIGURE 5. Codimension-two bifurcations near the corner. (*a*) $b_{21} < 0$, (*b*) $b_{21} > 0$.

For bifurcations on the axis, $x_c = 0, y_c \neq 0$. Here (18) gives two non-trival conditions, which can be solved to yield the bifurcation curve $\varepsilon = \mu^2/4$ and the critical point $y_c = -\mu/2$. As $y_c < 0$, the bifurcation occurs only for $\mu > 0$. From the theory of Brøns (1999) the type of bifurcation (bubble creation or bubble merging) is determined by the sign of $\psi_{xx}(0, y_c)/\psi_{xyy}(0, y_c)$, with two non-degeneracy conditions, $\psi_{xx}(0, y_c) \neq 0, \psi_{xyy}(0, y_c) \neq 0$. Here we get

$$\frac{\psi_{xx}(0, y_c)}{\psi_{xyy}(0, y_c)} = b_{21}, \quad \psi_{xx}(0, y_c) = -b_{21}\mu, \quad \psi_{xyy}(0, y_c) = -\mu. \tag{20}$$

The bifurcation at $\varepsilon = \mu^2/4$ is hence non-degenerate for $\mu \neq 0$ and is a bubble creation for $b_{21} > 0$ and a bubble merging for $b_{21} < 0$.

For bifurcations on the surface, $x_c \neq 0, y_c = 0$. However, proceeding as above shows that no critical point on the surface can be degenerate.

Finally, the degenerate critical point may be located away from the boundaries, and the bifurcation is a cusp bifurcation where a saddle and a centre merge and disappear. In this case all conditions in (18) are non-trivial and can be solved for x_c, y_c and ε in terms of μ. After some algebra one obtains the bifurcation curve and the critical point,

$$\varepsilon = \tfrac{9}{20}\mu^2 + O(\mu^3), \quad x_c = -\frac{3}{25}\frac{\mu^2}{b_{21}} + O(\mu^3), \quad y_c = -\tfrac{3}{10}\mu^2 + O(\mu^2). \tag{21}$$

As $x_c > 0$ and $y_c < 0$, this bifurcation can occur only when $b_{21} < 0$ and $\mu > 0$.

Combining these results, the bifurcation diagrams in figure 5 are obtained. Again, ρ and z may be interchanged, corresponding to assuming a_{21} small and $a_{12} \neq 0$, $a_{31} \neq 0$, and the axis and the surface in figure 5 are interchanged.

It should be noted that in establishing figure 5 we have only taken *local* bifurcations in account. However, one type of *global* codimension-one bifurcation also exists, namely the breaking of a saddle connection between three regular saddle points, see e.g. Bakker (1991). To examine whether such bifurcations do occur here one may start by noting that with the number of critical points available, a saddle connection can only involve two critical points on the boundary and one point away from the boundary. For the latter critical point we must have $\psi = 0$. It is not difficult to establish that this is not possible, and, having now considered all kinds of codimension-one bifurcation curves, the bifurcation diagrams are complete.

3. Numerics

3.1. *Numerical location of bifurcation sets*

For the numerical simulations we use the finite difference code developed at LIMSI/CNRS (Daube *et al.* 1985). At the free surface the following boundary conditions apply:

$$\psi = w = \frac{\partial \psi}{\partial r} = 0, \quad \frac{\partial^2 \psi}{\partial z^2} = 0. \tag{22}$$

For further information on the implementation for the flow in a cylinder with a fixed cover, including references, see Sørensen & Loc (1989) and Brøns *et al.* (1999).

Lengths are non-dimensionalized by the cylinder radius R, and the computational domain is $0 \leqslant r \leqslant 1, -h \leqslant z \leqslant 0$. Based on previous experience and the results we present in § 3.2 a grid size of $100 \times 100h$ for $h \geqslant 1$ and $100/h \times 100$ for $h < 1$ was found to be sufficient for analysing the parameter range of interest. Hence a larger computational effort is needed for values of h higher and lower than one.

Using the code, we obtain steady states by simulating until transients have died out. A state is accepted as being steady if the relative change of v in the (arbitrary) grid point (50, 50) has not been more than 10^{-13} for at least 250 time-step iterations. However, for the smallest aspect ratios and low Re the number of steps was reduced to 50 since the diffusion requirement

$$\Delta t < \tfrac{1}{8} Re \Delta r^2 \tag{23}$$

forces a reduction in the time-step Δt to avoid divergence, see Lopez (1990). In other parts of the parameter region Δt is limited by the convective stability criterion,

$$\Delta t < \frac{\Delta x}{U}, \tag{24}$$

where U is the velocity and x is the streamwise direction.

To establish the topology of a numerically determined ψ the critical points must be located. To locate critical points on the axis we proceed as in Brøns *et al.* (1999). From a Taylor expansion we get

$$\psi(\Delta r, z) = \psi(0, z) + \frac{\partial \psi}{\partial r}(0, z)\Delta r + \frac{1}{2}\frac{\partial^2 \psi}{\partial r^2}(0, z)\Delta r^2 + O(\Delta r^3). \tag{25}$$

Since ψ and $\partial\psi/\partial r$ are both zero on the axis we get to second order

$$w(0, z) = -\frac{\partial^2 \psi}{\partial r^2}(0, z) \approx \frac{2}{\Delta r^2}\psi(\Delta r, z). \tag{26}$$

Hence, we can locate critical points on the axis as zeros of $\psi_1(z) = \psi(\Delta r, z)$.

Let p_1 denote a value of z where ψ_1 attains a local extremum. Then a bifurcation of critical points as shown in figure 2(b, c) occurs at p_1 if $\psi(p_1) = 0$, for further details, see Brøns *et al.* (1999). This can be used for a least-squares fit of bifurcation curves. From a set of K simulations at different parameter pairs (h_i, Re_i) and corresponding values $\psi^{(i)}$ at an extremum $p_1^{(i)}$, we form the expression

$$C(h, Re) = c_{00} + c_{10}h + c_{01}Re + c_{20}h^2 + c_{02}Re^2 + c_{11}hRe, \tag{27}$$

and determine the c by minimizing

$$\sum_{i=1}^{K} (C(h_i, Re_i) - \psi^{(i)})^2. \tag{28}$$

A bifurcation curve is then found as $C(h, Re) = 0$.

For the present problem quadratic fits like (27) of the bifurcation curves turn out to suffice, except for a single case where a cubic fit is used. In general, other choices are of course possible.

To locate critical points on the surface we proceed similarly. In the Taylor expansion

$$\psi(r,-\Delta z)=\psi(r,0)-\frac{\partial\psi}{\partial z}(r,0)\Delta z+\frac{1}{2}\frac{\partial^2\psi}{\partial z^2}(r,0)\Delta z^2+O(\Delta z^3) \tag{29}$$

we use the boundary conditions (22) to obtain, again to second order,

$$u(r,0)=\frac{1}{r}\frac{\partial\psi}{\partial z}(r,0)\approx-\frac{1}{r}\frac{1}{\Delta z}\psi(r,-\Delta z). \tag{30}$$

Hence, critical points on the surface are the zeros of the stream function evaluated at the grid line below the surface, $\psi_2(r)=\psi(r,-\Delta z)$. Bifurcation curves for the creation and destruction of critical points on the surface are found by a fitting procedure on the basis of values of ψ_2 at extremum points p_2 analogous to the above.

For critical points in the corner the approach is slightly different. As shown in figure 4, either a critical point crosses the corner or a corner bubble is created when a bifurcation occurs. In both cases, the direction of the flow close to the corner reverses in the bifurcation. Since $\psi(0,0)=0$, the direction of the flow in the corner is given by the sign of $\psi(\Delta r,-\Delta z)$. Bifurcation occurs when this quantity is zero which we use as the basis for fitting bifurcation curves.

In this way all codimension-one bifurcation curves involving critical points on the axis and surface can be found. Finally, to determine cusp bifurcations as in figures 2(*c*) and 5(*a*) we proceed in a rather straightforward way. By visual inspection of the streamline pattern from a simulation close to a cusp bifurcation it was decided whether two critical points had merged or not. A bifurcation point is then determined as the mean value of two sufficiently close pairs of parameters for which the simulations are of distinct types. The bifurcation curves is obtained by connecting such points by a spline.

Our simulations indicate that the loss of stability occurs through a supercritical Hopf bifurcation. To locate the *Re* bifurcation point for fixed h we follow Daube & Sørensen (1989) and Brøns *et al.* (1999). For three slightly supercritical values of *Re* we determine the square a^2 of the amplitude of the oscillation at a fixed grid point. At a Hopf bifurcation a^2 locally scales linearly with the parameter. Making a least squares fit of a^2 as a function of *Re* the bifurcation point can be determined from an extrapolation to the point where $a^2=0$. The procedure is repeated for three different grid points, and the final bifurcation point is the mean value of the bifurcation points thus obtained.

3.2. *Numerical accuracy*

Previous comparisons of the results from the solver with experiments for the configuration with a fixed cover at $h=2$ (Sørensen & Christensen 1995; Sørensen & Loc 1989; Westergaard, Buchhave & Sørensen 1993) showed that a grid with $\Delta r=\Delta z=0.01$ gave results within experimental accuracy. For the same aspect ratio the influence of the grid on the topological bifurcations was investigated by Brøns *et al.* (1999). Here the investigation is extended to cover three other aspect ratios, $h=0.5, 1.5$ and 2.5. For each case three different grid sizes consisting of $50\times 50h, 100\times 100h$ and $200\times 200h$ for h larger than one and $50/h\times 50, 100/h\times 100$ and $200/h\times 200$ for h less than one are used. We refer to these grids as coarse, medium, and fine.

	Coarse	Medium	Fine
$h = 0.5$	240	240	240
$h = 1.5$	721	729	730
$h = 2.5$	1420	1459	1466

TABLE 1. Influence of mesh size on Re at topological bifurcation for fixed h. At $h = 0.5$, the bifurcation is the creation of a bubble in the corner, while for $h = 1.5$ and $h = 2.5$ it is the creation of a bubble on the axis.

	Fixed h	From curve
$h = 0.25$	1006	991
$h = 0.5$	240	256
$h = 1.5$	729	731
$h = 1.5$	1808	1799
$h = 2.5$	1459	1488

TABLE 2. Values of Re at bifurcation found at fixed values of h, compared with bifurcation points from two-parameter bifurcation curves.

	Coarse	Medium	Fine	Very fine
$h = 0.5$		6246		
$h = 0.75$	3859	3714	3769	3783
$h = 1.0$		2564		
$h = 1.5$	2460	2636	2640	
$h = 2.0$		2921		
$h = 2.5$	2499	2725	2787	
$h = 3.0$		3046		
$h = 3.5$		3316		
$h = 4.0$		3659		

TABLE 3. Stability limits in Re for different grids.

First, for a fixed value of h, we have performed three simulations at different Re and found the bifurcation measures, either $\psi(p_1), \psi_2(p_2)$, or $\psi(\Delta r, -\Delta z)$, as described in § 3.1. Making a least-squares linear fit, a bifurcation point Re is found when the measure is equal to zero. The simulations are performed close to and on both sides of a bifurcation.

In table 1 the results of this procedure using the coarse, medium and fine mesh are shown. The mesh size can have a significant effect on the bifurcation point on changing from the coarse to the medium mesh. However the maximum dispersion on changing from the medium to the fine mesh is only 7 in Re which is satisfying in this context.

Secondly, in table 2, we compare bifurcation points found with this method (first column) with bifurcation points at a bifurcation curve determined by the fitting procedure described in § 3.1. The latter points are found by inserting the value of h in the equation for the relevant bifurcation curve among those shown in figure 6. The deviation was found to be between 2 and 29 in Re which in the worst case is approximately 1% of the full Re interval considered here.

Finally, we test the grid influence on the stability limit. The result is shown in table 3. Again we see a large difference between the coarse and the medium grid, but results

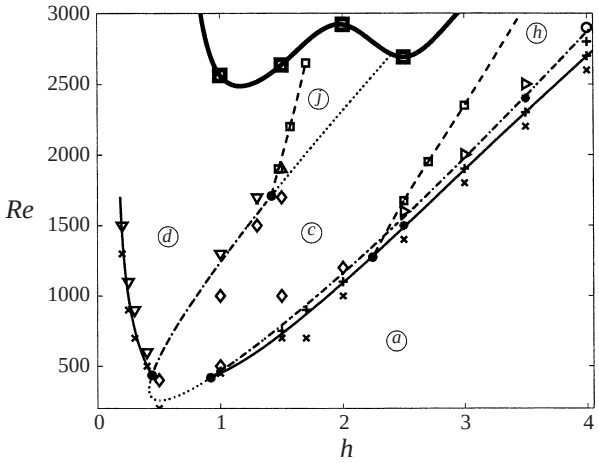

FIGURE 6. Overall bifurcation diagram. The labels refer to the classification in figure 1 and the symbols show parameter values where simulations are performed. ×, No bubbles, type (*a*); +, axis bubble, type (*b*); ◇, corner bubble, type (*c*); ▽, surface bubble, type (*d*); ∗, two axis bubbles, type (*e*); ○, axis bubble and corner bubble, type (*f*); ▷, corner bubble with inner structure, type (*h*); △, surface bubble and corner intrinsic saddle loop, type (*j*); □, points used for spline fits of cusp bifurcations; •, codimension-two points. The curves show the bifurcation sets obtained from fits of the data: ——, creation of a bubble on axis or surface; — · —, creation of corner bubble from axis bubble or surface bubble; – – –, cusp bifurcations, from figure 7 and 8; · · · · · ·, creation of corner bubble. The heavy curve is a spline fit of the stability limit based on data from table 3 using the medium grid. The corresponding symbols are the data points that are in the range of the diagram.

from the medium and fine grid agree within an Re range of 62. We have further tested the case at $h = 0.75$ on a very fine grid of size 310×250, and get only a small change from the result from the fine grid. This can also be compared with the results by Gelfgat *et al.* (1996*c*), who found the stability limit for the configuration with a cover co-rotating with the same angular velocity as the bottom. Their parameter values correspond to $h = 0.75$ here, and their result of $Re \approx 3840$ agrees with our finding within a reasonable accuracy.

4. Results

4.1. *The numerical bifurcation diagram*

Using the methods described in § 3.1, we have determined a set of codimension-one bifurcation curves in the (h, Re) parameter plane. The overall diagram is shown in figure 6 with finer details in figures 7, 8.

First, we have found a curve of corner bifurcation points in the form $C = 0$. The curve is found using the measure $\psi(\Delta r, -\Delta z)$ which does not distinguish between a corner bubble creation and a corner crossing. The type of bifurcation may change along the curve at codimension-two points. However, the curve goes smoothly through such points as it locally corresponds to $\varepsilon = 0$ in figure 5. Hence it makes sense to make a single smooth global fit of the curve. It is shown in figure 6 with dotted and dash-dotted parts.

Then a curve of axis bifurcations and a curve of surface bifurcations are determined, shown as full lines. The latter curves meet the corner bifurcation curves at codimension-two bifurcation points, $(h, Re) = (0.92, 419)$ and $(0.44, 436)$ respectively. From the topologies of the simulations performed close to these points we identify

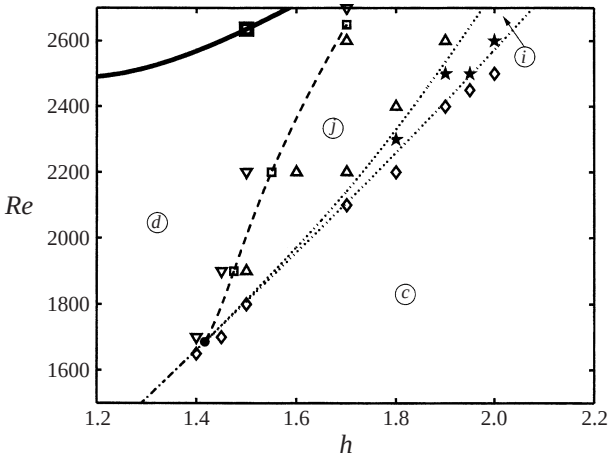

FIGURE 7. Detail of the bifurcation diagram. Same legend as figure 6, but ⋆, corner bubble with inner corner bubble, type (i); ····· (lower), creation of corner bubble; ····· (upper), axis stagnation points from inner and outer corner bubble merge and form a saddle loop.

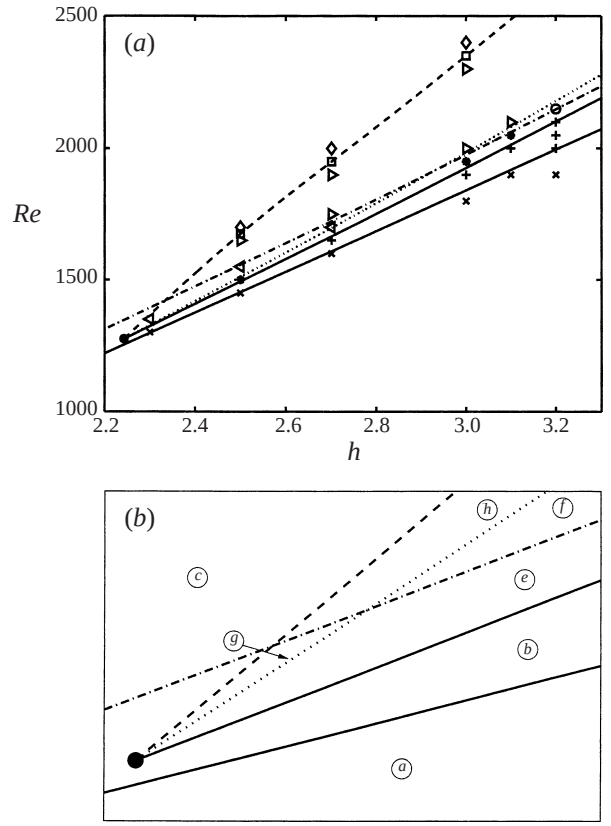

FIGURE 8. Detail of the bifurcation diagram: (*a*) to scale, (*b*) the qualitative arrangement of the bifurcation lines. Same legend as figure 6, but ◁, axis bubble with inner structure, type (*g*); —— (upper), creation of second axis bubble; ·····, two critical points on the axis merge and form an inner structure.

the type as in figure 5(*b*). The theory ensures that there are no further bifurcation curves originating at the codimension-two points.

The bifurcation diagram established to this point appears to imply the existence of a bifurcation curve separating type (*c*) from type (*j*). Clearly, this is not possible in a single codimension-one bifurcation, and further simulations show that very close to the curve there is a curve of axis bubble merging bifurcations (as in figure 2*c*). This curve, shown in figure 7, intersects the corner bifurcation curve at a codimension two point at $(h, Re) = (1.42, 1686)$. The type is figure 5(*b*). It follows that another bifurcation curve must emanate from the codimension-two point, namely a cusp bifurcation curve. This is indeed the case, and the curve is shown dashed in figures 6, 7.

Finally, proceeding as above, we have located three more bifurcation curves: an axis bubble creation curve, an axis bubble merging curve, and a cusp bifurcation curve. They meet at a codimension-two point at $(h, Re) = (2.24, 1275)$ as shown in figure 8. The codimension-two point is of the type shown in figure 2(*d*).

This completes our investigation of the topologies of the flow. A small part of the diagram was also found numerically by Valentine & Jahnke (1994) and our results essentially agree. It should be noted, however, that the diagram is not complete. For low values of h and high values of Re there is a series of bifurcations leading to a cellular flow structure, as exemplified by (*v*) and (*w*) in figure 1. These structures are outside the scope of the present study, and we only mention that Valentine & Jahnke (1994) determined some of the bifurcation curves leading to the cellular structure. Undoubtedly, there is a complicated topological bifurcation structure in this parameter region.

We have included an estimation of the stability limit in figure 6. A spline fit of the nine Hopf bifurcation points obtained with the medium grid (table 3) is shown as a heavy curve. The four bifurcation points that are in the range of the diagram are also shown. The curve agrees with a similar curve obtained by Gelfgat *et al.* (1996*a*) which includes the range $0 \leqslant \gamma \leqslant 1.5$. Note that their definition of γ is twice the one we use.

4.2. *Comparison with experiments*

Spohn, Mory & Hopfinger (1993, henceforth denoted SMH) have performed a series of experiments with the flow in the steady domain. Using a fluorescent dye injected at the cylinder axis on the free surface the structures close to the axis are visualized by a laser light sheet. The findings were summarized in a bifurcation diagram similar to figure 6. However the classification of the flow patterns is not as detailed as the one presented here. SMH denote a bubble 'attached' if one critical point is on the surface regardless of the position of the other critical point. Hence, they do not distinguish between type (*c*) and type (*d*). Further, a bubble is denoted 'detached' if both critical points are on the axis, and 'long' if it has an inner structure like types (*g*) and (*h*).

From the diagram we have extracted three bifurcation curves: transitions from no bubble to a detached bubble, from a detached bubble to an attached bubble, and from an attached bubble to a long attached bubble. In our terminology these correspond to axis bubble creation, corner crossing, and cusp bifurcation, respectively.

Rather than using the bifurcation curves loosely sketched by SMH, we have estimated the bifurcation points directly from the measurement points indicated in their bifurcation diagram, assuming that a bifurcation occurs midway between two measurements with a different topology. The resulting bifurcation points are shown as symbols in figure 9.

We find good agreement for the axis bubble creation when $h > 1$, while the results deviate somewhat for $0.5 < h < 1$. The experimental corner crossing curve is system-

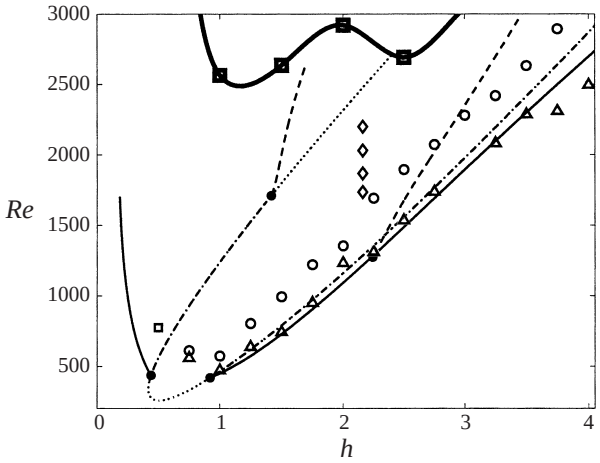

FIGURE 9. Comparison between numerical results and measurements by Spohn *et al.* (1993). The curves are from figure 6, while symbols are experimentally determined bifurcation points: △, axis bubble creation, corresponding to the full line, ○, corner crossing bifurcation, corresponding to the dash-dotted line; ◇, inner structure in corner bubble vanishes in a cusp bifurcation, corresponding to the dashed line; □, experimental codimension-two point.

atically located at higher values of Re than the numerical one. The two curves meet at a codimension-two point as in our model, but the location is different. In fact, our bifurcation diagram contains two codimension-two points for Re close to 500. There must be another bifurcation curve emanating from the codimension-two point, but the experimental data do not contain sufficient information to determine it.

The cusp curves do not agree very well, although their general locations in the diagram are comparable.

SMH have also found a region with a 'long detached bubble', type (g). This is located around the tiny region where we have found it (see figure 8), but it is much larger.

The stability limit found by SMH is approximately $Re = 2100$ independent of h when $h < 2.5$, and rises monotonically for higher values of h, ending at $Re \approx 2800$ at $h = 4$, the highest aspect ratio considered. These values are substantially lower than our findings shown in table 3 and figure 6.

5. Conclusions

We have demonstrated the power of a topological approach to the identification of patterns in flows. The building blocks of a two-parameter bifurcation diagram are curves of codimension-one bifurcations which meet at codimension-two points. The bifurcation curves can be found from a relatively small set of simulations and from the topological catalogue of codimension-two points the total diagram can be patched together with confidence.

In the specific application, the flow in a cylinder with a rotating bottom and a free surface, the agreement between numerics and experiment is not as good as for the flow with a fixed cover (Brøns *et al.* 1999). The discrepancy of the stability limits is not surprising: in the model oscillations of the free surface are not possible, and surface waves clearly play a role in the transition to periodic flow. Hence one should indeed expect that the real instability occurs at an earlier stage. Furthermore, in the

flow with a fixed cover, Escudier (1984) finds experimentally that the transition to periodic flow is always to a three-dimensional flow when $h > 3.1$. One can expect that in the present case three-dimensional effects are even more pronounced.

The differences between computations and experiment may also partly be ascribed to the resolution of the visualization being not nearly as good as in the fixed cover case. Due to light reflections from the surface and the injection tube, the region close to the corner is rather blurred. This makes it very difficult to locate critical points here and hence to precisely find bifurcations at the corner.

However, the main problem is clearly that the modelling of the surface as flat and stress free is a strong simplification, especially for small aspect ratios. In addition to including free-surface motion, the effect of a surface film was considered by Lopez & Chen (1998) in their computational study of the flow. The streamline topology was shown to depend on the physical characteristics of the film.

We conclude that the dynamics of the free surface has an influence on the flow topology, but much of the structure of the bifurcation diagram is reproduced by our model. The topological classification depends only on the axis and the surface being iso-curves of ψ and not on the fluid dynamics. Hence, if surface effects are included in the mathematical model, the same building blocks for the topology will be relevant. If surface effects are small, the bifurcation diagram will persist qualitatively, although the quantitative shape of the bifurcation diagram will change. However, if surface effects result in major changes in the overall flow, the bifurcation diagram may be altered significantly.

The flow topologies (*i*) and (*j*) are not found at all by SMH. Case (*j*) is probably very difficult to identify experimentally since visualization of the quite small saddle loop requires that tracer is somehow transported into the loop. Case (*i*) is only predicted to exist in a very narrow parameter region. In general, we find a number of very narrow regions in the bifurcation diagram which will be almost impossible to find experimentally. Nevertheless, these regions are important to establish computationally, since they are essential parts of a consistent bifurcation diagram.

The types of codimension-one bifurcation curves found by SMH are the same as we find from the topological analysis. However, the way SMH merge these at codimension-two points does not in all cases agree with the theory. This is a subtle matter since one can easily think of bifurcation diagrams in a neighbourhood of a codimension-two point which are topologically feasible, but, by a specific bifurcation analysis as in § 2.2 can be shown to be impossible.

Hence, the present approach should be helpful as a guide for further experimental investigations.

We are grateful to Andreas Spohn for some very useful comments about the experiment.

REFERENCES

Bakker, P. G. 1991 *Bifurcations in Flow Patterns*. Klüver.

Brøns, M. 1994 Topological fluid dynamics of interfacial flows. *Phys. Fluids* **6**, 2730–2737.

Brøns, M. 1999 Topological fluid mechanics of axisymmetric flows. In *Simulation and Identification of Organized Structures in Flows* (ed. J. N. Sørensen, E. J. Hopfinger & N. Aubry), pp. 213–222. Klüwer.

Brøns, M. & Hartnack, J. N. 1999 Streamline topologies near simple degenerate critical points in two-dimensional flow away from boundaries. *Phys. Fluids* **11**, 314–324.

Brøns, M., Voigt, L. K. & Sørensen, J. N. 1999 Streamline topology of steady axisymmetric vortex breakdown in a cylinder with co- and counter-rotating end-covers. *J. Fluid Mech.* **401**, 275–292.

Daube, O., Loc, T. P., Monet, P. & Coutanceau, M. 1985 Ecoulement instationaire décollé d'un fluide incompressible autour d'un profil: une comparaison theorié-experience. *AGARD CP* 366.

Daube, O. & Sørensen, J. N. 1989 Simulation numerique de l'ecoulement periodique axisymmetrique dans une cavite cylindrique. *C. R. l'Acad. Sci.* II **308**, 463–469.

Escudier, M. P. 1984 Observations of the flow produced in a cylindrical container by a rotating endwall. *Exps. Fluids* **2**, 189–196.

Escudier, M. P. & Cullen, L. M. 1996 Flow of a shear-thinning liquid in a cylindrical container with a rotating end wall. *Expl Thermal Fluid Sci.* **12**, 381–387.

Gelfgat, A. Y., Bar-Yoseph, P. Z. & Solan, A. 1996*a* Confined swirling flow simulation using spectral Galerkin and finite volume methods. In *ASME Fluids Engineering Summer Division Meeting*. FED vol. 238, pp. 105–112.

Gelfgat, A. Y., Bar-Yoseph, P. Z. & Solan, A. 1996*b* Stability of confined swirling flow with and without vortex breakdown. *J. Fluid Mech.* **311**, 1–36.

Gelfgat, A. Y., Bar-Yoseph, P. Z. & Solan, A. 1996*c* Steady states and oscillatory instability of swirling flow in a cylinder with rotating top and bottom. *Phys. Fluids* **8**, 2614–2625.

Goldstein, H. 1950 *Classical Mechanics.* Addison-Wesley.

Jahnke, C. C. & Valentine, D. T. 1998 Recirculation zones in a cylindrical container. *Trans. ASME: Fluids Engng* **120**, 680–684.

Lopez, J. M. 1990 Axisymmetric vortex breakdown part 1. Confined swirling flow. *J. Fluid Mech.* **221**, 533–552.

Lopez, J. M. & Chen, J. 1998 Coupling between a viscoelastic gas/liquid interface and a swirling vortex flow. *Trans. ASME: J. Fluids Engng* **120**, 655–661.

Mullin, T., Kobine, J. J., Tavener, S. J. & Cliffe, K. A. 2000 On the creation of stagnation points near straight and sloped walls. *Phys. Fluids* **12**, 425–431.

Pereira, J. C. F. & Sousa, J. M. M. 1999 Confined vortex breakdown generated by a rotating cone. *J. Fluid Mech.* **385**, 287–323.

Ronnenberg, B. 1977 Ein selbstjustierendes 3-Komponenten-Laserdoppler-Anemometer nach dem Vergleichsverfaren, angewandt auf Untersuchungen in einer stationären zylinder-symmetrischen Drehströmgebiet. Bericht 19. Max-Planck-Institut für Strömungsforschung, Göttingen.

Sørensen, J. N. & Christensen, E. A. 1995 Direct numerical simulation of rotating fluid flow in a closed cylinder. *Phys. Fluids* **7**, 764–778.

Sørensen, J. N. & Loc, T. P. 1989 High-order Axisymmetric Navier–Stokes Code: Description and Evaluation of Boundary Conditions. *Intl J. Numer. Meth. Fluids* **9**, 1517–1537.

Spohn, A., Mory, M. & Hopfinger, E. J. 1993 Observations of vortex breakdown in an open cylindrical container with a rotating bottom. *Exps. Fluids* **14**, 70–77 (referred to herein as SMH).

Tsitverblit, N. 1993 Vortex breakdown in a cylindrical container in the light of continuation of a steady solution. *Fluid Dyn. Res.* **11**, 19–35.

Valentine, D. T. & Jahnke, C. C. 1994 Flows induced in a cylinder with both end walls rotating. *Phys. Fluids* **6**, 2702–2710.

Vogel, H. U. 1968 Experimentelle ergebnisse über die laminäre Strömung in einem zylindriche Gehäuse mit darin rotierender Scheibe. Bericht 6. Max-Planck-Institut für Strömungs-forschung, Göttingen.

Westergaard, C., Buchhave, P. & Sørensen, J. N. 1993 PIV measurements of turbulent and chaotic structures in a rotating flow using an optical correlator. In *Laser Techniques and Applications in Fluid Mechanics* (ed. R. J. Adrain). Springer.

Xue, S. C., Phan-Thien, N. & Tanner, R. I. 1999 Fully three-dimensional, time-dependent numerical simulations of Newtonian and viscoelastic swirling flows in a confined cylinder part I. Method and steady flows. *J. Non-Newtonian Fluid Mech.* **87**, 337–367.